ACS APPLIED MATERIALS & INTERFACES

Research Article

www.acsami.org

Fabrication of α-Fe_2O_3 Nanorod/RGO Composite: A Novel Hybrid Photocatalyst for Phenol Degradation

Gajendra Kumar Pradhan, Deepak Kumar Padhi, and K. M. Parida*

Colloids and Materials Chemistry Department, CSIR-Institute of Minerals & Materials Technology, Bhubaneswar-751013, Odisha, India

ABSTRACT: We report herein the fabrication of a hematite nanorod−graphene composite (α-Fe_2O_3 nanorod/RGO) via a facile template-free hydrothermal route with an aim to improve the photocatalytic efficiency of the α-Fe_2O_3 nanorod. The structural and morphological characterizations of the as-prepared composites were carried out using X-ray diffraction, Raman spectra, X-ray photoelectron spectroscopy, scanning electron microscopy, transmission electron microscopy, N_2 adsorption−desorption, etc. The α-Fe_2O_3 nanorods were well-decorated on the surface of the graphene sheets, which helps in electron transfer from α-Fe_2O_3 to graphene and hence can delay the recombination process, leading to the improvement in photocatalytic activity. The composite containing 5 wt % RGO and α-Fe_2O_3 nanorods shows a 4-fold enhancement in the photocatalytic activity. The performance of photocatalytic activity was discussed in light of surface area, interaction between nanorods and graphene nanosheets, synergism between α-Fe_2O_3 nanorods and RGO sheets, light-harvesting properties of the composites, photoluminescence spectra, photocurrent measurement, and hydroxyl radical formation.

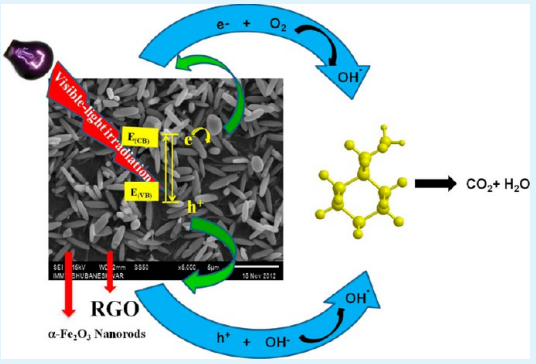

KEYWORDS: *hydrothermal, nanorod, composite, photocatalysis, recombination, hydroxyl radical*

1. INTRODUCTION

Since the pioneering work on "photocatalytic water splitting on TiO_2 electrodes" by Fujisima and Honda, extensive research has been carried out for the photocatalytic oxidation of various aqueous and gaseous pollutants.[1] With the gradual development of various photocatalytic semiconductor materials, such as TiO_2, ZnO, CdS, etc., α-Fe_2O_3 is considered as one of the challenging materials in this category.[2−11] α-Fe_2O_3 has high absorptive power in the red light of the visible range, which is around 43% in the solar spectrum. However, the charge carrier recombination lowers its efficiency, which alternately limits the photocatalytic performance. Several steps have been taken to improve its efficiency, such as heteroatom doping, architectural control, heterostructure, composites with other semiconductors, etc.[12−22]

On the other hand, graphene, a two-dimensional single-layer sheet of sp^2-hybridized carbon atoms, remains one of the emerging materials having superior properties, such as high electrical conductivity, high surface area, optically transparent, etc.[23−25] This enforces the photocatalytic researcher to make a hybrid with other semiconductor metal oxides. The primary role of graphene toward this composite semiconductor photocatalyst system is to delocalize the photogenerated electron through its π network, which inhibits the recombination process and hence improves the photocatalytic performance. In recent years, various graphene-based semiconductor metal oxide nanocomposites, such as TiO_2, ZnO, SnO_2, Co_3O_4, MnO_2, CdS, CdSe, Fe_2O_3, etc., have been developed for photocatalytic applications.[26−34] Meng et al. reported the enhancement of photocatalytic water oxidation activity due to incorporation of α-Fe_2O_3 nanoparticles on the reduced graphene oxide sheet.[31] Hou et al. reported the α-Fe_2O_3 nanorod/graphene/$BiV_{1-x}Mo_xO_4$ for photoelectrochemical water splitting.[32] The He group reported the fabrication of nanocrystalline α-Fe_2O_3 by coupling phosphate-functionalized graphene and studied their photocatalytic activity.[33] Photodegradation of toluene over a spindle-shaped α-Fe_2O_3/graphene oxide composite was studied by Li et al.[34] All the groups claimed that the enhancement in photocatalytic activity is due to the fast transfer of photogenerated electrons from α-Fe_2O_3 to the RGO nanosheets. In the present work, the principal aim is to find out the effect of structural, optical, and electronic properties of the α-Fe_2O_3 nanorod−graphene composite in delaying the flash recombination period of electrons−holes, which alternately improves their photocatalytic efficiency.

Previously, we have reported various photocatalytic materials, such as TiO_2, α-Fe_2O_3, ZnO/Fe_2O_3, and S,N-codoped α-Fe_2O_3, for the decomposition of organic pollutants.[35−38] In our α-Fe_2O_3 nanorod paper, we have compared the photocatalytic performance between nanospheres with one-dimensional nanorods. The superiority of the nanorod was well-explained

Received: June 26, 2013
Accepted: August 20, 2013
Published: August 20, 2013

by electron channelization through the one-dimensional nanostructure.[36] To further improve the separation of electron−hole, leading to improved photocatalytic performance, here, we have fabricated α-Fe_2O_3 nanorod/RGO composite. The α-Fe_2O_3 nanorod/RGO composite was prepared by a hydrothermal technique without using any template and implemented them for the decomposition of a non-self-sensitizing pollutant, that is, phenol, by a photocatalytic process.

2. MATERIALS AND METHODS

2.1. Materials. All the chemicals and reagents are of analytical grade and used without further purification. Iron(III) chloride hexahydrate, diammonium hydrogen phosphate, and deionized water were used for the sample preparation. Commercial Fe_2O_3 was used for comparison of catalytic activity with the prepared nanocomposites.

2.2. Synthesis of Graphene Oxide (GO). Graphene oxide was synthesized by the modified Hummers method.[39] In a typical method, 0.5 g of graphite powder along with 0.5 g of $NaNO_3$ was suspended in 23 mL of concentrated H_2SO_4. It was allowed to stir for 15 min, and the suspension was transferred to an ice bath, followed by slow addition of 4 g of $KMnO_4$ till the solution of the color changes to purple-green. It was then placed in a water bath to maintain the temperature around 40 °C. Afterwards, it was allowed to stir for 90 min, followed by addition of 50 mL of deionized water, and again stirred for 20 min. About 6 mL of 30% H_2O_2 was added slowly to produce a golden-brown solution. A 50 mL portion of deionized water was then added to it, and the resultant solution was centrifuged and washed several times with deionized water to adjust the pH to 6. Finally, the obtained product was dried at 80 °C for 24 h.

2.3. Synthesis of α-Fe_2O_3 Nanorods. α-Fe_2O_3 nanorods were synthesized by our previously reported method with minor modification.[36] $(NH_4)_2HPO_4$ and $FeCl_3{\cdot}6H_2O$ solutions were separately prepared and mixed in a stoichiometric ratio. The homogeneous yellow solution was transferred to a Teflon-lined autoclave, followed by hydrothermal treatment at 180 °C for 36 h. After the treatment, the products were collected by centrifugation, filtered, washed several times with deionized water, and dried at 110 °C for overnight. The sample was designated as 0GFO.

2.4. Synthesis of α-Fe_2O_3/RGO Composites. In a typical experiment, a stoichiometric amount of $(NH_4)_2HPO_4$ was added to an aqueous solution of $FeCl_3{\cdot}6H_2O$ under vigorous stirring until a yellow homogeneous solution was obtained. In another pot, GO was dispersed in deionized water for 1 h. Both solutions were mixed and transferred to a Teflon-lined autoclave, followed by hydrothermal treatment at 180 °C for 36 h. After the treatment, the products were collected by centrifugation, filtered, washed several times with deionized water, and dried at 110 °C for overnight. The 1, 3, 5, and 7 wt % GO-loaded samples are designated as 1GFO, 3GFO, 5GFO, and 7GFO. The details of the synthesis of α-Fe_2O_3/RGO composites are schematically presented in Scheme 1.

2.5. Characterization. Phase identification was carried out using a PANalytical X-ray diffractometer with Mo Kα radiation (λ = 0.70932 Å) in the 2θ range from 10 to 40°. Surface morphology of the samples was studied through a transmission electronic microscope (FEI, TECNAI G^2 20, TWIN, Philips) operating at 200 kV. The samples for electron microscopy were prepared by dispersing in ethanol and coating a very dilute suspension on carbon-coated Cu grids. TEM images were recorded by using a Gutan CCD camera. The surface morphologies were also examined through a scanning electron microscope (SEM, Hitachi S-3400N) by collecting secondary electron images at 15 kV. The samples were coated with gold to make the surface conducting during SEM measurement. Raman spectra were recorded in a backscattering configuration at room temperature using a RENISHAW InVia Raman spectrometer. An argon ion laser was used as the excitation source at 540 nm. The electronic states of Fe were examined by X-ray photoelectron spectroscopy (XPS, Kratos Axis 165 with a dual anode (Mg and Al) apparatus) using the Mg Kα source. All the binding energy values were calibrated by using the contaminant carbon (C 1s = 284.9 eV) as a reference. Photocurrent measurement was performed by a conventional Pyrex electrochemical cell consisting of a prepared electrode, a platinum wire as a counter electrode (1 mm in diameter, 15 mm in length), and a Ag/AgCl reference electrode. The pH of the solution was kept at 6, and the cell was filled with an aqueous solution of 0.1 M Na_2SO_4. Prior to electrochemical measurements, nitrogen was purged into the electrolyte, and the potential of the electrode was controlled by a potentiostat (Versastat 3, Princeton Applied Research) with a 300 W Xe lamp. The OH radical formation was studied by replacing phenol with 5×10^{-4} M terephthalic acid (TPA) and 2×10^{-3} M NaOH with the same amount of photocatalysts. The PL spectra were measured on a PerkinElemer LS-55 fluorescence spectrometer with an excitation at 315 nm light. The photoluminescence spectra of all the photocatalysts were carried out with the same LS-55 fluorescence spectrometer.

Scheme 1. Schematic Representation of the Fabrication of α-Fe_2O_3 Nanorod/RGO Composite

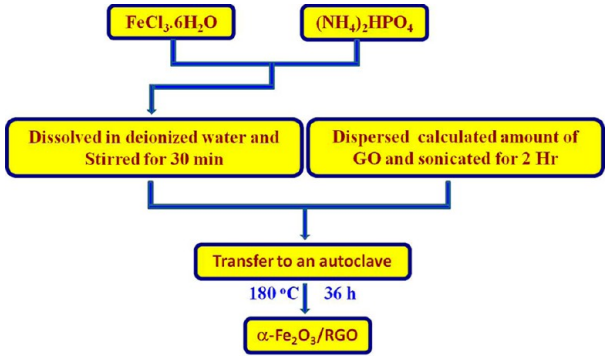

2.6. Photocatalytic Reaction. The photoefficiency of all synthesized catalysts was tested toward degradation of phenol under solar radiation. In a typical experiment, 20 mg of photocatalyst with 20 mL of 10 ppm phenol solution was taken in a 100 mL closed Pyrex flask. The solutions were exposed to visible light irradiation in an irradiation chamber (BS-02, Germany) for 2 h. After irradiation, the suspension was centrifuged and the concentration of the supernatant solution was analyzed quantitatively at 504 nm (λ_{max} for phenol) using a Cary-100 (Varian, Australia) spectrophotometer. All the catalytic results were reproducible with ±2% variation.

3. RESULTS AND DISCUSSION

3.1. XRD. Figure 1 shows the XRD patterns of α-Fe_2O_3/RGO nanocomposites. The diffraction patterns obtained for 0GFO are indexed to α-Fe_2O_3 [JCPDS 13-534]. The indexing planes are (012), (104), (110), (202), (024), (116), (214), and (300). Similar indexing patterns are also obtained for 1GFO, 3GFO, 5GFO, and 7GFO. No significant changes occur in the XRD patterns between the neat α-Fe_2O_3 and RGO modified α-Fe_2O_3. That means the phase purity of α-Fe_2O_3 is maintained after the composite formation with RGO, which is preferred for its photocatalytic activity. It is also observed that no corresponding characteristics peaks were found for RGO in the XRD pattern of α-Fe_2O_3/RGO composites up to a 5 wt % loading. This is reasonably explained by its low amount, low diffraction pattern intensity, and breaking of its regular lamellar arrangement by the intercalation of α-Fe_2O_3 nanorods in between its stacked 2D monolayers, which leads to exfoliation and wrapping of RGO sheets during composite formation.[40] This indicates the good incorporation of α-Fe_2O_3 nanorods in between the sp^2-hybridized carbon monolayer of RGO sheets up to 5 wt % of loading. In the case of 7 wt % loaded α-Fe_2O_3, the characteristic peak for RGO was observed at 2θ ~ 24−31°.

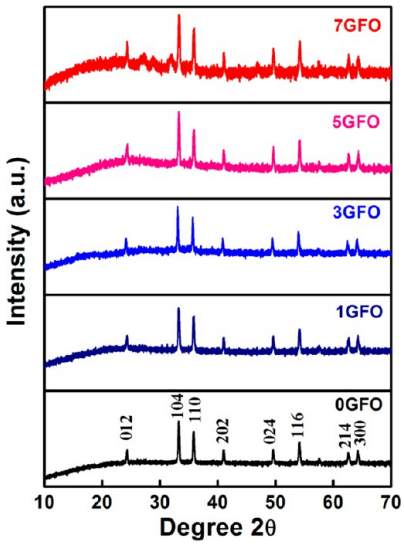

Figure 1. XRD patterns of 0GFO, 1GFO, 3GFO, 5GFO, and 7GFO photocatalysts.

It is probably due to the sufficient exfoliation of RGO sheets by the attached α-Fe_2O_3 nanorods.[41]

3.2. Electron Microscopy. SEM, FESEM, and TEM analysis of the photocatalysts were done to identify the shape, morphology, and size of the particles. Figure 2 illustrates the SEM images of 0GFO and 5GFO photocatalysts. It is clearly observed that the α-Fe_2O_3 particles are rod-shaped and well-dispersed on the surface of GO. Figure 2b represents the 5 wt % GO-loaded α-Fe_2O_3 (5GFO) where the nanorods are well-dispersed on the graphene sheets. This means that there is direct interaction between every nanorod with the RGO sheet, which is favorable for photocatalytic application. Figure 3a–c shows the TEM micrographs of 0GFO, GO, and 5GFO, respectively. 0GFO's have a nanorod morphology with a well-dispersed structure, which is consistent with the SEM micrograph. The rods are elongated longitudinally to a finite dimension. Previously, we designed the α-Fe_2O_3 nanorod by the same hydrothermal technique with a heating temperature of 220 °C and obtained nanorods with a length of 294 nm.[36] In the present context, the hydrothermal temperature is changed

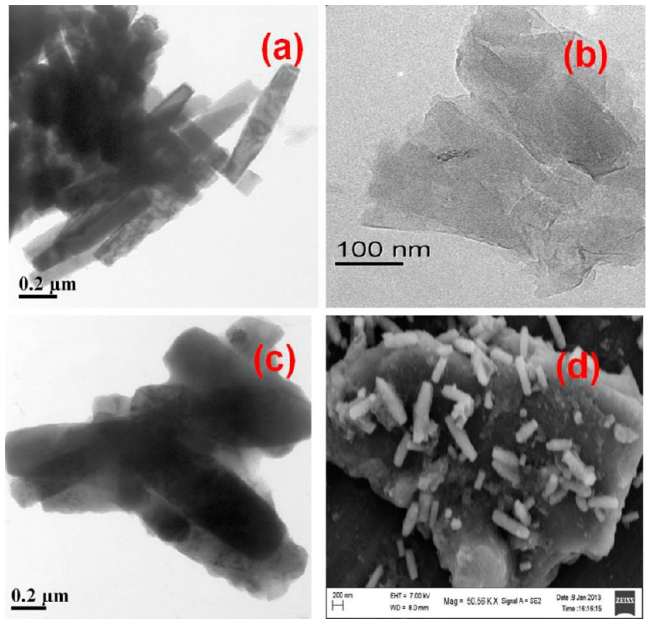

Figure 3. TEM micrographs of (a) 0GFO, (b) GO, and (c) 5GFO photocatalysts. (d) FESEM micrograph of 5GFO.

to 180 °C and the nanorods are obtained with an average length of 700 nm. It means that the temperature has a significant role during the growth of nanorods. The reduced structure of RGO (Figure 3b) has a flat surface morphology and a sheet structure. The sheets always remain stacked in the absence of any foreign material. In the composite case (Figure 3c), the α-Fe_2O_3 nanorods are well-decorated on the surface of the RGO sheets. Here, by the introduction of α-Fe_2O_3 nanorods, the sheets are exfoliated and intact with the nanorods providing a composite material. Figure 3d represents the FESEM micrograph of the 5GFO photocatayst. Here, the α-Fe_2O_3 nanorods are well-placed on the surface of the RGO sheet. The intimate contact between α-Fe_2O_3 nanorods and RGO sheets remains one of the advantages in the photocatalytic activity.

3.3. Optical Characterization. To know the optical absorption, UV–vis DRS has been taken using a Cary 100

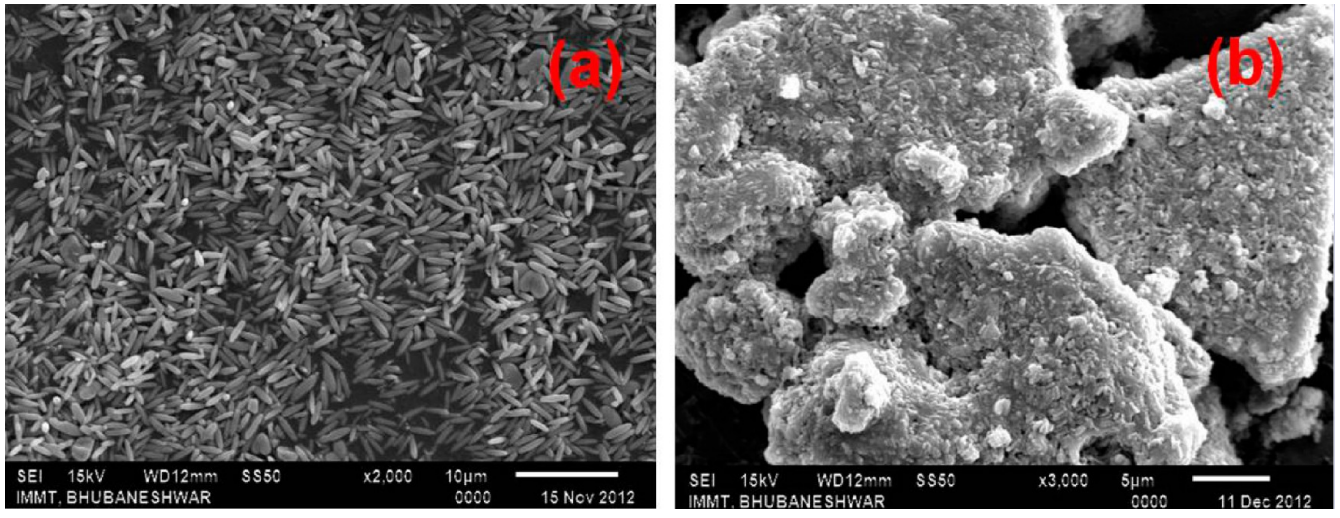

Figure 2. SEM micrographs of (a) 0GFO and (b) 5GFO photocatalysts.

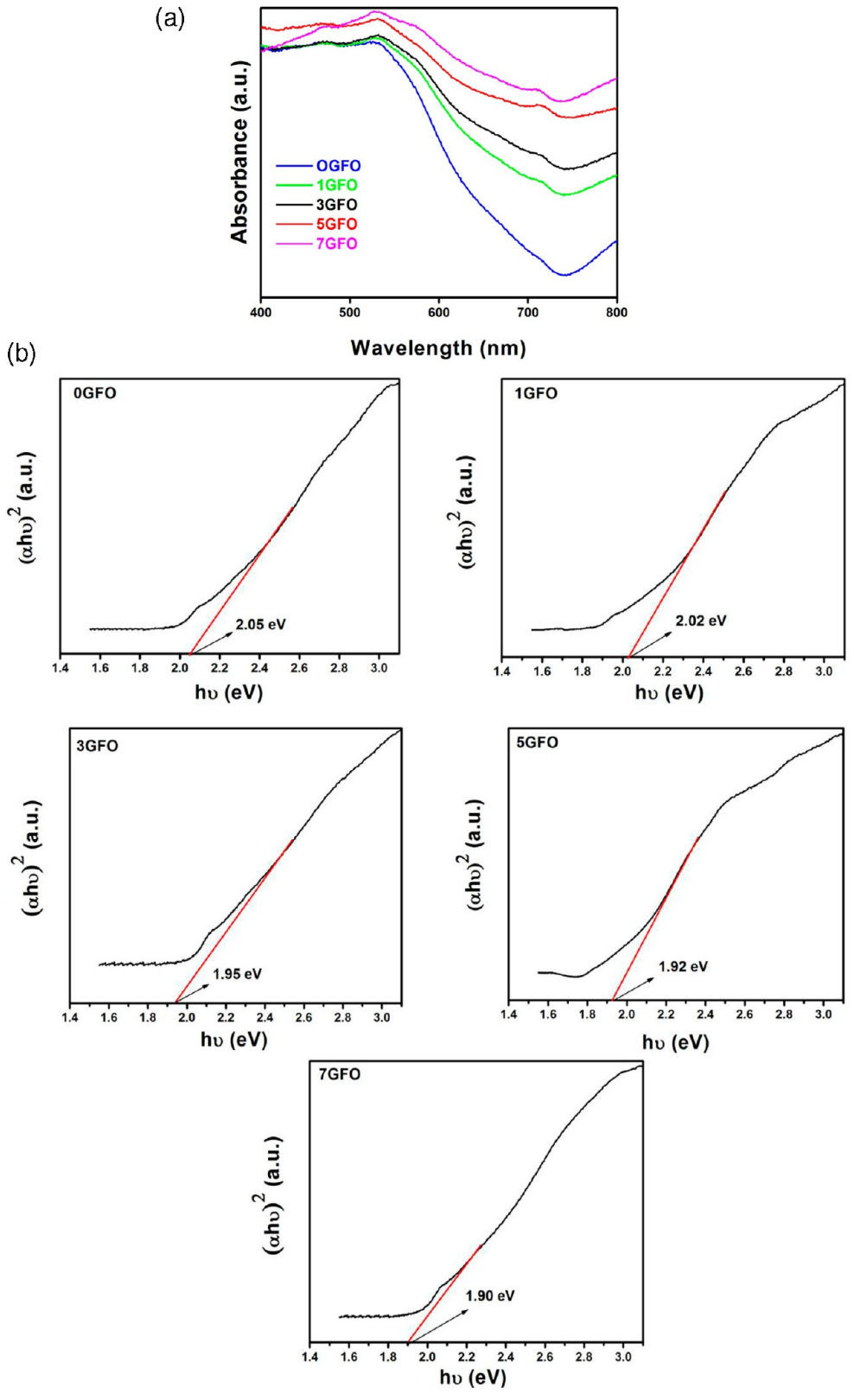

Figure 4. (a) Optical absorbance spectra of the 0GFO, 1GFO, 3GFO, 5GFO, and 7GFO. (b) Estimated band-gap energy of the 0GFO, 1GFO, 3GFO, 5GFO, and 7GFO.

UV−vis spectrophotometer. Figure 4 shows the DRS spectra of all the synthesized photocatalysts. The UV−visible absorption spectra of 0GFO shows an absorption band at 526 nm corresponding to the $2(^6A_1) \rightarrow (^4T_1)$ ligand field transition of Fe^{3+}, whereas, in case of 5GFO, the absorption edge is larger than 526 nm.[42] 5GFO also shows an increase in the absorption spectra intensity in the visible light region compared to 0GFO. This is due to the presence of blackbody properties of RGO

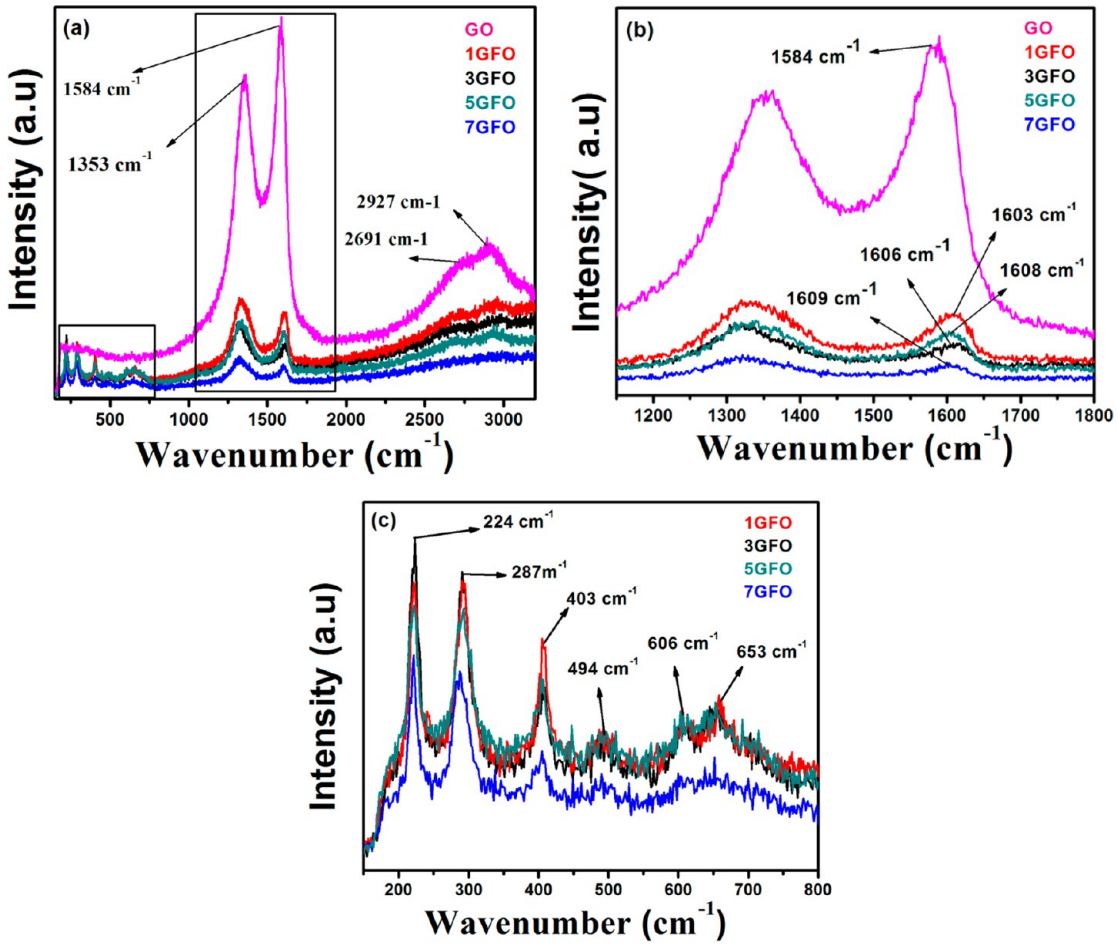

Figure 5. (a) Raman spectra of GO and α-Fe_2O_3/RGO composite. (b) Raman "G" band position of GO and α-Fe_2O_3/RGO composite. (c) The fundamental Raman vibration of α-Fe_2O_3 in α-Fe_2O_3/RGO composite.

sheets.[43] That means that the deoxygenated surface of GO is obtained during the composite formation by hydrothermal treatment, which indicates the conversion of GO to RGO. These interpretations also suggest that the presence of RGO indirectly modifies the fundamental process of electron−hole pair formation of α-Fe_2O_3 nanorods by increasing its surface electric charge during the photochemical process.[43]

The band-gap energy of all the prepared α-Fe_2O_3/RGO nanocomposites were calculated by using the following equation[44]

$$ah\nu = A(h\nu - E_g)^n$$

where a, n, A, and E_g are the absorption coefficient, light frequency, proportionality constant, and band-gap energy, respectively, and n describes the type of the transition in a semiconductor, that is, $n = 1/2$ for direct transition and $n = 2$ for indirect transition. In our case, the value of n for all the prepared samples was taken as 1/2. That means that the optical transition of α-Fe_2O_3/RGO nanocomposites is directly allowed. The band gap of all the synthesized photocatalysts is shown in Figure 4b. It is estimated from the plot of $(\alpha h\nu)^n$ versus $h\nu$ by extrapolating the straight line to the X axis intercept. The band-gap energies of 0GFO, 1GFO, 3GFO, 5GFO, and 7GFO were found to be 2.05, 2.02, 1.95, 1.94, and 1.90 eV, respectively. As evidenced from the band-gap energy estimation of prepared photocatalysts, the introduction of RGO does not strongly affect the optical absorption property of iron oxide, whereas its presence shifts the absorption edge of all samples toward the red region.

3.4. Raman Spectra. Figure 5a shows the Raman spectra of GO and GO-loaded α-Fe_2O_3. In the case of GO, the two peaks observed at 1353 and 1584 cm^{-1} correspond to its D and G bands, respectively.[45] Here, the appearance of the D band is due to the defects as well as disordered atomic arrangement caused by the sp^3-carbon atom. The G band can be assigned to the plane vibration of the sp^2-carbon atom in the two-dimensional lattice. In addition to this, the appearance of two weak peaks at 2691 and 2927 cm^{-1} can be assigned to the 2D band, which originates from the second-order Raman scattering process.[46] However, the Raman spectrum of GO-loaded α-Fe_2O_3 contains both "D and G" bands of GO along with all the fundamental Raman vibration of α-Fe_2O_3 (Figure 5c); that is, 224 cm^{-1} corresponds to A_{1g} symmetry; 287, 403, 494, and 606 cm^{-1} for E_g symmetry, and 653 cm^{-1} for disorder symmetry, respectively. This confirms the composite formation between GO and α-Fe_2O_3. In addition to that, the I_D/I_G values of 1GFO, 3GFO, 5GFO, and 7GFO are larger than the I_D/I_G value of GO (Table 1), which confirms the reduction of GO to RGO. The I_D/I_G value of GO is 0.8587, whereas this value is highest in the case of 5GFO, that is, 1.3326. This larger I_D/I_G value of the α-Fe_2O_3/RGO composite also reveals a decrease in the average sp^2 domain of GO after hydrothermal reduction.[47] The shifting in the G band position (Figure 5b) of the α-Fe_2O_3/RGO composite toward higher frequency by ~25 cm^{-1} compared to

dx.doi.org/10.1021/am402487h | ACS Appl. Mater. Interfaces 2013, 5, 9101−9110

Table 1. Intensity Ratio of "D" and "G" Bands (I_D/I_G) and Variation in the G Band Position of GO and α-Fe_2O_3/RGO Composite

material	position of "G" band (cm^{-1})	I_D/I_G
GO	1584	0.8587 ± 0.0015
1GFO	1603	1.1459 ± 0.0073
3GFO	1606	1.1681 ± 0.0026
5GFO	1608	1.3326 ± 0.0059
7GFO	1609	1.1912 ± 0.0064

GO clearly suggests the incorporation of α-Fe_2O_3 nanorods in between the graphene layer, which is consistent with TEM analysis.

3.5. XPS. XPS of the 5GFO photocatalyst was carried out to establish the oxidation state and electronic environment of C, O, and Fe. Figure 6a depicts the high-resolution XPS spectrum of C 1s. It is clearly seen that the peak observed at 284 eV (A) corresponds to the sp^2 aromatic C−C bond. The peak B in Figure 6a indicates a considerable degree of oxidation and the presence of different oxygen-containing groups in RGO, and for the sake of convenience, it was deconvoluted into two peaks. The first peak appeared at 288.5 (standard BE for C═O is 287.9 eV) was assigned to the C═O group, whereas the later one at 290.5 eV is due to the satellite peak (Figure 6b).[48,49] The only peak at 529.8 eV (Figure 6c) is assigned to O^{2-} forming an oxide with iron, which normally appeared at 529−529.4 eV.[50] Generally, the XPS of Fe $2p_{3/2}$ for the oxide state of iron(III) is observed with a binding energy (BE) value between 710.6 and 711 eV.[50−53] In the present case (Figure 6d), the peaks that appeared at 711 and 723.9 eV for Fe $2p_{3/2}$ and Fe $2p_{1/2}$, respectively, are ascribed to +3 oxidation states of iron in α-Fe_2O_3. The shifting of XPS peaks for carbon, iron, and oxygen from their normal value confirms the close interaction between RGO and α-Fe_2O_3 and the formation of nanocomposites.

3.6. N_2 Adsorption−Desorption. To know the porous nature of the material, N_2 adsorption−desorption of all the photocatalysts was carried out by the BET method at 77 K. The specific surface area (SSA), pore diameter, and pore volume of all the photocatalysts are presented in Table 2. The SSA of the

Table 2. Textural Properties of All the Synthesized Samples

catalysts	surface area (m^2/g)	pore volume (cm^3/g)	pore diameter (nm)
0GFO	9.6 ± 1.2	0.07 ± 0.015	29.1 ± 2.7
1GFO	20 ± 2.3	0.07 ± 0.019	26.4 ± 2.2
3GFO	22.8 ± 1.8	0.08 ± 0.023	16.9 ± 1.9
5GFO	46 ± 2.5	0.15 ± 0.016	10.5 ± 1.6
7GFO	29.5 ± 2.6	0.12 ± 0.024	16.0 ± 2.4

plane α-Fe_2O_3 (0GFO) is found to be 9.6 m^2/g. However, after composite formation with graphene, the SSA increases gradually and reaches a maximum of 46 m^2/g in the case of 5GFO. The increase of SSA may be ascribed to exfoliation and cross-linking points between RGO and α-Fe_2O_3 nanorods up to a 5 wt % loading.[55] However, in 7GFO, the SSA decreases to 29.5 m^2/g. It may be due to sufficient exfoliation of graphene sheets, which leads to wrapping and folding over α-Fe_2O_3 nanorods. The pore size distribution measurement indicates that all the samples have a pronounced mesoporosity of a narrow pore size distribution with an average pore size of 29.1, 26.4, 16.9, 16, and 10.5 nm and a pore volume of 0.07, 0.07, 0.08, 0.12, and 0.15 cm^3/g, respectively, for 0GFO, 1GFO, 3GFO, 5GFO, and 7GFO.

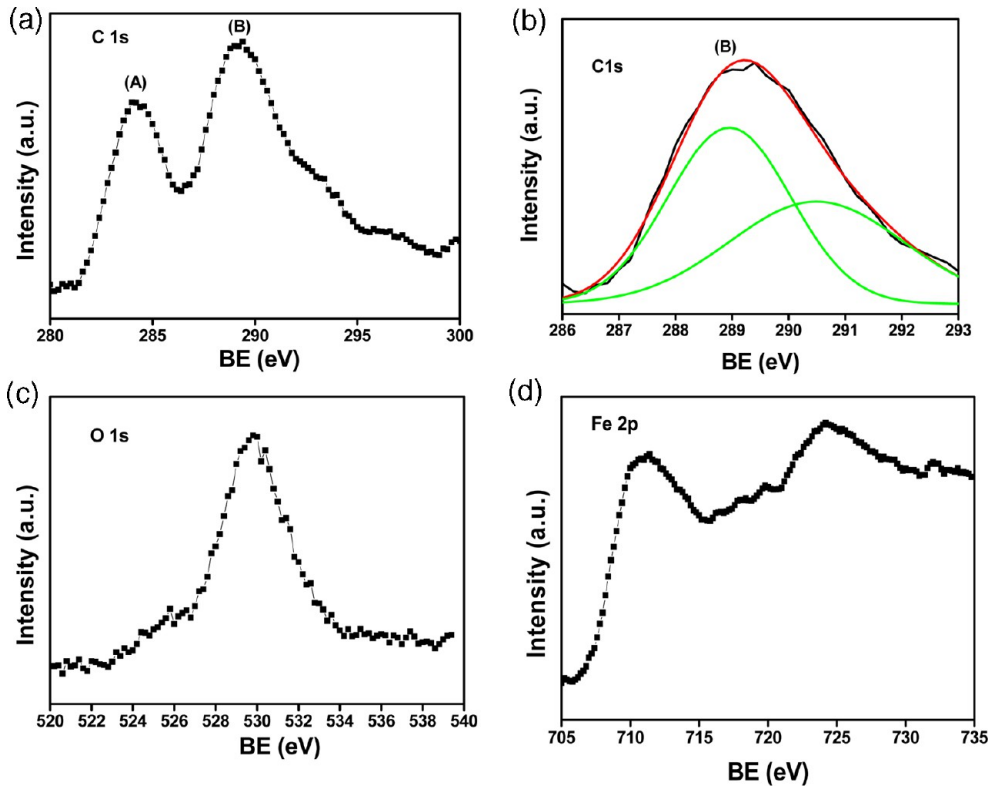

Figure 6. (a) High-resolution XPS spectrum of C 1s. (b) Deconvolution of peak B in C 1s spectrum. (c) High-resolution XPS spectrum of O 1s. (d) High-resolution XPS spectrum of Fe 2p.

3.7. Photocurrent Measurement. Figure 7 represents the photocurrent plot of 0GFO and 5GFO. From the plot, it is

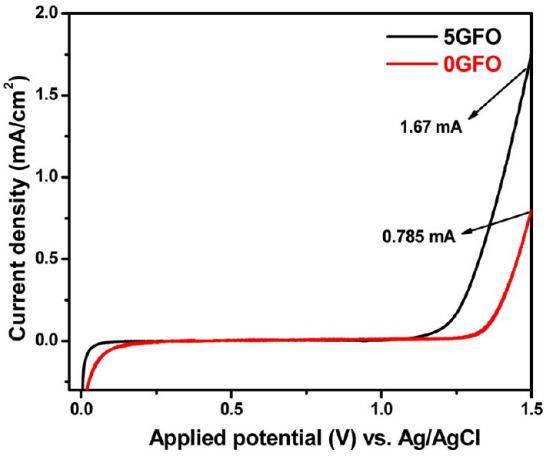

Figure 7. Photocurrent–potential curves under visible light illumination of 0GFO and 5GFO photocatalysts.

observed that 0GFO (α-Fe_2O_3) generates an anodic current with applied bias. This generation of anodic photocurrent implies that both 0GFO and 5GFO are of n-type semiconductor. It is also observed that 0GFO gives a photocurrent of 0.785 mA/cm^2 under visible light irradiation (λ > 420 nm). However, under the same condition, 5GFO gives a photocurrent of 1.67 mA/cm^2, which is more than 2 times greater than that of 0GFO. That means, after illumination of photons, a higher number of electrons are generated from 5GFO, leading to high photocurrent generation. This can be explained by the following points, that is: (1) Because of the extensive π–π conjugation linkage between the sp^2-hybridized carbon of graphene, it possesses high mobility and also acts as an electron sink.[56,57] This outstanding property of graphene is beneficial for accepting the photoinduced electron of α-Fe_2O_3 and also plays an important role for suppressing the electron–hole recombination by channelizing the photogenerated electron through its surface, which eventually enhances the photocurrent generation. (2) Good distribution of α-Fe_2O_3 nanorods on the surface of graphene leads to the development of better contact between RGO and α-Fe_2O_3 nanorods, which is responsible for better transportation of photoinduced electrons from α-Fe_2O_3 to RGO sheets and drastically increases the photocurrent generation. In other words, in the case of the composite, good allocation and attachments of α-Fe_2O_3 nanorods over the RGO monolayer creates a platform to utilize the photogenerated electrons that arise from α-Fe_2O_3 nanorods in the photochemical process. Hence, the photocatalytic efficiency of 5GFO is significantly increased compared to that of OGFO for phenol degradation under visible light irradiation.

3.8. Structural Changes of α-Fe_2O_3 upon Complexation with RGO. As evidenced from XRD analysis, the presence of RGO does not effect the crystal orientation of α-Fe_2O_3. The crystalinity as well as phase purity of α-Fe_2O_3 is well-maintained up to a 7 wt % RGO loading. Only a slight broadening of the most characteristic peak (104) of α-Fe_2O_3 was observed on RGO loading. From electron microscopic analysis, the decoration and incorporation of α-Fe_2O_3 nanorods on RGO sheets allow us to draw the following conclusions, that is: (1) The presence of RGO strongly inhibits the agglomeration of α-Fe_2O_3 nanorods, and simultaneously, the stacking of RGO sheets is also avoided. (2) The good attachment through the strong interaction between α-Fe_2O_3 nanorods and RGO leads to an increase in the surface area. (3) The length of synthesized α-Fe_2O_3 is 700 nm, which decreases to 600 nm after the formation of the α-Fe_2O_3/RGO (5GFO) composite. In the case of the composite, the strong interaction of α-Fe_2O_3 nanorods with RGO gives a good platform for better transportation of photoexcited electrons to RGO, which is more beneficial for the minimization of electron–hole recombination and enhancing the photocatalytic activity

3.9. Photocatalytic Reaction. In the application part, degradation of phenol has been carried out to establish the superior catalytic acitivity of the α-Fe_2O_3/RGO nanocomposite. The percentage of phenol degradation was examined as a function of different photocatalysts. The reaction time was optimized using the 5GFO photocatalyst (Figure 8). The

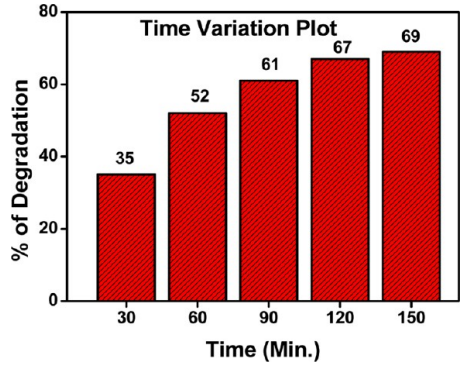

Figure 8. Time variation plot of the 5GFO photocatalyst.

samples were collected at different time intervals, such as 30, 60, 90, 120, and 150 min, and monitored in the UV–vis spectrophotometer. It is observed that the rate of degradation rises up to 120 min. No marginal enhancement was obtained after 120 min. Therefore, the photocatalytic experiments were performed at 120 min.

Figure 9 shows the percentage of phenol degradation as a function of different photocatalysts. Phenol with the photo-

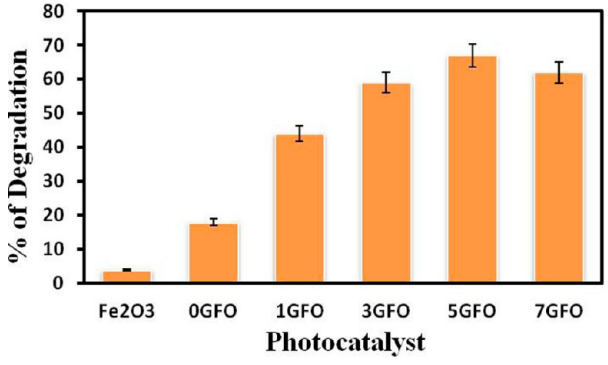

Figure 9. Photocatalytic degradation of phenol over all the synthesized photocatalysts.

catalyst was directly exposed to the light in the chamber for 2 h. It has been observed that there is hardly degradation of phenol without the photocatalyst. However, when α-Fe_2O_3 (0GFO) was present, the percentage of degradation was 18%. The degradation percentage dramatically increased in the α-Fe_2O_3–RGO composites. It showed 44, 59, 67, and 62% of degradation

dx.doi.org/10.1021/am402487h | ACS Appl. Mater. Interfaces 2013, 5, 9101–9110

of phenol with 1GFO, 3GFO, 5GFO, and 7GFO, respectively. For comparison, it was also tested with commercial hematite (Fe_2O_3). The photocatalytic performance exhibited a trend: Fe_2O_3 < 0GFO < 1GFO < 3GFO < 7GFO < 5GFO.

3.9.1. Mechanism of Hydroxyl Radical Formation and Phenol Degradation. Photocatalytic degradation was generally operated by the action of hydroxyl radicals formed during the reaction. In the present case, when the α-Fe_2O_3 nanorod/RGO composite was illuminated with light greater than the band-gap energy, electrons are excited from the valence band to the conduction band, leaving a hole in the valence band. The hydroxyl groups present on the surface of the photocatalyst react with the photogenerated hole to produce hydroxyl radicals. Similarly, the dissolved oxygen interacts with photogenerated electrons, forming a superoxide, which again reacts with a proton, yielding the hydroperoxyl radicals, followed by the formation of hydrogen peroxide. A hydroxyl radical was also produced by the attack of a photogenerated electron to the hydrogen peroxide.[37,38] The phenol oxidation and degradation mechanism was well-studied by many researchers.[58,59] Phenol was oxidized to hydroxyl phenols by the oxidizing species formed during the process. The hydroxyl phenol compounds then break down to the corresponding acid and finally converted to CO_2 and water.

3.9.2. Factors Affecting the Photocatalytic Reaction. Electron−hole recombination is a major drawback for most of the semiconducting materials in photocatalysis. That is why neat α-Fe_2O_3 shows comparatively low activity in comparison to the α-Fe_2O_3/RGO composite. In the case of neat α-Fe_2O_3, the energy difference between the conduction band and the valence band is 2.2 eV, where the chances of recombination are high. However, when α-Fe_2O_3 is placed on the surface of RGO sheets, there is a strong interaction and development of a synergistic effect between α-Fe_2O_3 and RGO. This leads to delaying of recombination of excited photoelectrons with holes. Here, RGO acts as an electron acceptor center as well as it can easily channelize them through its flat sp^2-hybridized carbon network. Therefore, in the composite case (α-Fe_2O_3/RGO), the carrier recombination is delayed; hence, the percentage of photodegradation increases. The presence of RGO also improves the light-harvesting capacity of α-Fe_2O_3 nanorods, which alternately improves the photocatalytic activity. On the basis of our results and discussion, we have arrived at evidence to establish the superiority of composites compared to neat α-Fe_2O_3 material, such as the (a) higher number of active sites for the accommodation of substrate molecules, (b) generation of high photocurrent, (c) lowering of electron−hole recombination, (d) and formation of a sufficient number of hydroxyl radicals.

3.9.2.1. Greater Number of Active Sites for the Accommodation of Substrate Molecules. Surface area has a significant role in catalysis and also in photocatalytic activity. Higher surface area has a greater number of active sites and hence can accommodate a greater number of substrate molecules. The surface area of 0GFO is only 9.6 m^2/g and can accommodate minimum substrate molecules and hence could decompose only 18% phenol. The surface area is increased gradually by modifying with GO, and thus, the photocatalytic performance also gradually increases. It was maximum at 5GFO (46 m^2/g) and gives a maximum percentage of phenol decomposition.

3.9.2.2. Generation of High Photocurrent. Photocurrent is directly proportional to generation of photoelectron density. As discussed in the previous section, the generation of photoelectrons in the 5GFO composite leads to high photocurrent as compared to 0GFO. This implies that the flow of photoelectrons is more and hence can be utilized in the redox process. That is why a higher percentage of photocatalytic activity is observed in 5GFO as compared to 0GFO.

3.9.2.3. Lowering of Electron−Hole Recombination. Photoluminescence spectra have been used to inspect the mobility of the charge carriers to the surface as well as the recombination process involving the electron−hole pairs in semiconductor particles. PL emission results from the radiative recombination of excited electrons and holes. In other words, it is an essential requirement of a good photocatalyst to have minimum electron−hole recombination. To study the recombination of charge carriers, PL studies of synthesized materials have been undertaken. PL emission intensity is directly related to recombination of excited electrons and holes.[60,61] Figure 10 shows the photoluminescence spectra of

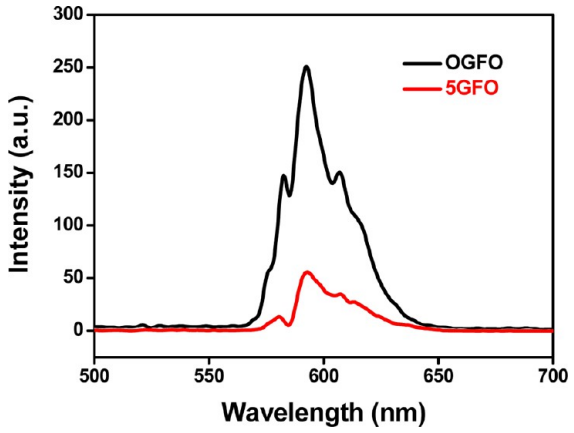

Figure 10. Photoluminescence spectra of 0GFO and 5GFO photocatalysts.

synthesized photocatalysts. It means 0GFO with strong PL intensity has high recombination of charge carriers, whereas 5RGO has weak intensity. The weak PL intensity of 5GFO may arise due to the well-decorated α-Fe_2O_3 nanorods on the RGO sheet, resulting in the decolorization of photoexcited electrons through the sp^2-bonded carbon network. This delays the electrons−holes recombination process and hence is utilized in the redox reaction, leading to improved photocatalytic activity.

3.9.2.4. Hydroxyl Radical Formation. As the hydroxyl radical performs the key role for the decomposition of the organic pollutants, it is necessary to investigate the amount of hydroxyl radicals produced by each photocatalyst. Thus, there is a technique to establish the formation of hydroxyl radicals using terephthalic acid (TA) as a probe molecule. In this method, TA was directly attacked by a OH radical, forming 2-hydroxyterephthalic acid (TAOH), which gives a fluorescence signal at 426 nm.[61−63] Figure 11 depicts the fluorescent signal of all the photocatalysts after reacting with TA solution. The fluorescent intensity is linearly related to the number of hydroxyl radicals formed by the photocatalysts. It means the higher the generation of hydroxyl radicals is, the higher the yield of TAOH will be and hence the more intense the fluorescence peak will be. Thus, 5GFO with the highest intensity confirms the generation of a greater number of hydroxyl radicals compared to other photocatalysts. The fluorescence intensity

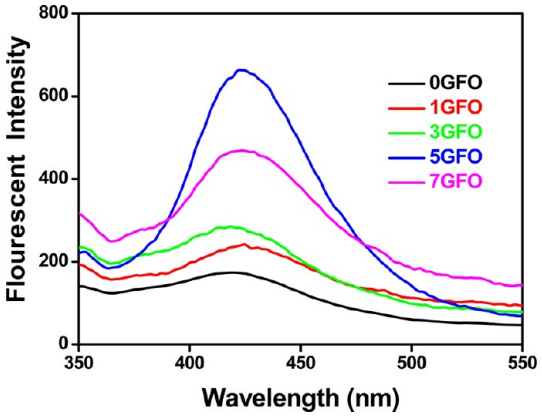

Figure 11. PL spectral changes with the visible light irradiation time for all the catalysts in a 5×10^{-5} M basic solution of terephthalic acid.

follows the trend (i.e., 0GFO < 1GFO < 3GFO < 7GFO < 5GFO) of photocatalytic performance of all the photocatalysts.

4. CONCLUSIONS

In summary, we have successfully fabricated α-Fe_2O_3 nanorod/RGO composites by a hydrothermal technique without using any template, which shows enhanced photocatalytic activity compared to the neat α-Fe_2O_3 nanorod. The α-Fe_2O_3 nanorod containing 5 wt % graphene exhibits 67% of phenol degradation, which is 4-fold higher than that of the neat sample. Taking into account the presence of RGO, the enhanced performance of the composite materials was established by (a) the utilization of a greater number of photoelectrons ascertained from photocurrent measurement, (b) the lowering of electron−hole recombination found from PL measurement, and (c) the proficient fast production of the OH radical by PL measurement in the presence of scavengers. The high activity was ascribed to strong interaction and development of a synergestic effect between the α-Fe_2O_3 nanorod and RGO. This composite material seems to be a promising candidate for solar cell as well as fuel cell applications.

AUTHOR INFORMATION

Corresponding Author

*E-mail: paridakulamani@yahoo.com.

Notes

The authors declare no competing financial interest.

ACKNOWLEDGMENTS

All the authors acknowledge Prof. B. K. Mishra, Director, IMMT, Bhubaneswar, for his constant encouragement and permission to publish the paper. Financial support from BRNS to Dr. K. Padhi is highly appreciated. We are also very grateful to CSIR for providing an SRF fellowship to G. K. Pradhan.

REFERENCES

(1) Fujishima, A.; Honda, K. *Nature* **1972**, *238*, 37−38.
(2) Kumar, S. G.; Devi, L. G. *J. Phys. Chem. A* **2011**, *115*, 13211−13241.
(3) Dutta, S.; Patra, A. K.; De, S.; Bhaumik, A.; Saha, B. *ACS Appl. Mater. Interfaces* **2012**, *4*, 1560−1564.
(4) Wojtoniszak, M.; Dolat, D.; Morawski, A.; Mijowska, E. *Nanoscale Res. Lett.* **2012**, *7*, 235.
(5) Lazar, M. A.; Daoud, W. A. *RSC Adv.* **2013**, *3*, 4130−4140.
(6) Cho, S.; Jang, J. W.; Lee, J. S.; Lee, K. H. *Nanoscale* **2012**, *4*, 2066−2071.
(7) Lu, Y.; Lin, Y.; Xie, T.; Chen, L.; Yi, S.; Wang, D. *ACS Appl. Mater. Interfaces* **2013**, *5*, 4017−4020.
(8) Chen, X.; Shangguan, W. *Front. Energy* **2013**, *7*, 111−118.
(9) Biswal, N.; Parida, K. M. *Int. J. Hydrogen Energy* **2013**, *38*, 1267−1277.
(10) Harris, C.; Kamat, P. V. *ACS Nano* **2009**, *3*, 682−690.
(11) Holmes, M. A.; Townsend, T. K.; Osterloh, F. E. *Chem. Commun.* **2012**, *48*, 371−373.
(12) Cesar, I.; Kay, A.; Martinez, J. A. G.; Gratzel, M. *J. Am. Chem. Soc.* **2006**, *128*, 4582.
(13) Luo, W.; Wang, D.; Wang, F.; Liu, T.; Cai, J.; Zhang, L.; Liu, Y. *Appl. Phys. Lett.* **2009**, *94*, 202507.
(14) Wu, N.; Wang, J.; Tafen, D. N.; Wang, H.; Zheng, J. G.; Lewis, J. P.; Liu, X.; Leonard, S. S.; Manivannan, A. *J. Am. Chem. Soc.* **2010**, *132*, 6679−6685.
(15) Mu, J.; Shao, C.; Guo, Z.; Zhang, Z.; Zhang, M.; Zhang, P.; Chen, B.; Liu, Y. *ACS Appl. Mater. Interfaces* **2011**, *3*, 590.
(16) Jennings, J. R.; Ghicov, A.; Peter, L. M.; Schmuki, P.; Walker, A. B. *J. Am. Chem. Soc.* **2008**, *130*, 13364.
(17) Zhu, K.; Neale, N. R.; Miedaner, A.; Frank, A. J. *Nano Lett.* **2007**, *7*, 69.
(18) Mor, G. K.; Shankar, K.; Paulose, M.; Varghese, O. K.; Grimes, C. A. *Nano Lett.* **2006**, *6*, 215.
(19) Niu, M.; Huang, F.; Cui, L.; Huang, P.; Yu, Y.; Wang, Y. *ACS Nano* **2010**, *4*, 681−688.
(20) Wang, L.; Wei, H.; Fan, Y.; Gu, X.; Zhan, J. *J. Phys. Chem. C* **2009**, *113*, 14119−14125.
(21) Guo, Y.; Zhang, G.; Liu, J.; Zhang, Y. *RSC Adv.* **2013**, *3*, 2963−2970.
(22) Águila, M. J. R.; González, M. P. E.; Mendoza, M. E.; Gonzáleza, R. S.; Madeira, H. Y. *Surf. Interface Anal.* **2012**, *44*, 484−490.
(23) Zhu, Y.; Murali, S.; Cai, W.; Li, X.; Suk, J. W.; Potts, J. R.; Ruoff, R. S. *Adv. Mater.* **2010**, *22*, 3906−3924.
(24) Huang, X.; Yin, Z.; Wu, S.; Qi, X.; He, Q.; Zhang, Q.; Yan, Q.; Boey, F.; Zhang, H. *Small* **2011**, *7*, 1876−1902.
(25) Nair, R. R.; Blake, P.; Grigorenko, A. N.; Novoselov, K. S.; Booth, T. J.; Stauber, T.; Peres, N. M. R.; Geim, A. K. *Science* **2008**, *320*, 1308.
(26) Huang, Q.; Tian, S.; Zeng, D.; Wang, X.; Song, W.; Li, Y.; Xiao, W.; Xie, C. *ACS Catal.* **2013**, *3*, 1477−1485.
(27) Luo, Q.-P.; Yu, X.-Y.; Lei, B.-X.; Chen, H.-Y.; Kuang, D.-B.; Su, C.-Y. *J. Phys. Chem. C* **2012**, *116*, 8111−8117.
(28) Seema, H.; Kemp, K. C.; Chandra, V.; Kim, K. S. *Nanotechnology* **2012**, *23*, 355705.
(29) Liu, X.; Pan, L.; Lv, T.; Zhu, G.; Sun, Z.; Sun, C. *Chem. Commun.* **2011**, *47*, 11984−11986.
(30) Oh, W. C.; Chen, M.; Cho, K.; Kim, C.; Meng, Z.; Zhu, L. *Chin. J. Catal.* **2011**, *32*, 1577−1583.
(31) Meng, F.; Li, J.; Cushing, S. K.; Bright, J.; Zhi, M.; Rowley, J. D.; Hong, Z.; Manivannan, A.; Bristow, A. D.; Wu, N. *ACS Catal.* **2013**, *3*, 746−751.
(32) Hou, Y.; Zuo, F.; Dagg, A.; Feng, P. *Nano Lett.* **2012**, *12*, 6464−6473.
(33) He, L.; Jing, L.; Li, Z.; Sun, W.; Liu, C. *RSC Adv.* **2013**, *3*, 7438−7444.
(34) Li, H.; Zhao, Q.; Zhu, Z.; Tade, M.; Li, X.; Liu, S. *J. Nanopart. Res.* **2013**, *15*, 1670.
(35) Naik, B.; Parida, K. M.; Gopinath, C. S. *J. Phys. Chem. C* **2010**, *114*, 19473−19482.
(36) Pradhan, G. K.; Parida, K. M. *ACS Appl. Mater. Interfaces* **2011**, *3*, 317−323.
(37) Pradhan, G. K.; Martha, S.; Parida, K. M. *ACS Appl. Mater. Interfaces* **2012**, *4*, 707−713.
(38) Pradhan, G. K.; Sahu, N.; Parida, K. M. *RSC Adv.* **2013**, *3*, 7912−7920.
(39) Hummers, W. S.; Offeman, R. E. *J. Am. Chem. Soc.* **1958**, *80*, 1339−1339.

(40) Xu, C.; Wang, X.; Zhu, J.; Yang, X.; Lu, L. *J. Mater. Chem.* **2008**, *18*, 5625−5629.
(41) Liu, S. Y.; Xie, J.; Pan, Q.; Wu, C. Y.; Cao, G. S.; Zhu, T. J.; Zhao, X. B. *Int. J. Electrochem. Sci.* **2012**, *7*, 354−362.
(42) Cornell, R. M.; Schwertmann, U. *The Iron Oxide Book*, 2nd ed.; Wiley-VCH: Weinheim, Germany, 2003; p 147.
(43) Zhang, L. W.; Fu, H. B.; Zhu, Y. F. *Adv. Funct. Mater.* **2008**, *18*, 2180−2189.
(44) Parida, K. M.; Nashim, A.; Mahanta, S. K. *Dalton Trans.* **2011**, *40*, 12839−12845.
(45) Mkhoyan, K. A.; Contryman, A. W.; Silcox, J.; Stewart, D. A.; Eda, G.; Mattevi, C.; Miller, S.; Chhowalla, M. *Nano Lett.* **2009**, *9*, 1058.
(46) Tuinstra, F.; Koenig, J. L. *J. Chem. Phys.* **1970**, *53*, 1126.
(47) Shah, M. S. A. S.; Park, A. R.; Zhang, K.; Park, J. H.; Yoo, P. J. *ACS Appl. Mater. Interfaces* **2012**, *4*, 3893−3901.
(48) Onyiriukat, C. E. *Chem. Mater.* **1993**, *5*, 798−801.
(49) Fu, R.; Yoshizawa, N.; Dresselhaus, M. S.; Dresselhaus, G.; Satcher, J. H.; Baumann, T. F. *Langmuir* **2002**, *18*, 10100−10104.
(50) Yamashita, T.; Hayes, P. *Appl. Surf. Sci.* **2008**, *254*, 2441−2449.
(51) Wagner, C. D.; Riggs, W. M.; Davis, L. E.; Muilenberg, J. F. *Handbook of X-ray Photoelectron Spectroscopy*; PerkinElmer: Eden Prairie, MN, 1979.
(52) Bhargaba, G.; Gouzman, I.; Chun, C. M.; Ramanarayanan, T. A.; Bernasek, S. L. *Appl. Surf. Sci.* **2007**, *253*, 4322−4329.
(53) Grosvenor, A. P.; Kobe, B. A.; Biesinger, M. C.; Mclntyre, N. S. *Surf. Interface Anal.* **2004**, *36*, 1564−1574.
(54) Luan, V. H.; Tien, H. N.; Hoa, L. T.; Hien, N. T. M.; Oh, E. S.; Chung, J.; Kim, E. J.; Choi, W.; Kong, B. S.; Hur, S. H. *J. Mater. Chem. A* **2013**, *1*, 208−211.
(55) Shah, M. S. A. S.; Zhang, K.; Park, A. R.; Kim, K. S.; Park, N. G.; Park, J. H.; Yoo, P. J. *Nanoscale* **2013**, *7*, 5093−5101.
(56) Zhang, N.; Zhang, Y.; Xu, Y. J. *Nanoscale* **2012**, *4*, 5792−5813.
(57) Liqiang, J.; Yichuna, Q.; Baiqi, W.; Shudan, L.; Baojiang, J.; Libin, Y.; Wei, F.; Honggang, F.; Jiazhong, S. *Sol. Energy Mater. Sol. Cells* **2006**, *90*, 1773−1787.
(58) Sobczynski, A.; Duczmal, L.; Zmudzinski, W. *J. Mol. Catal. A: Chem.* **2004**, *213*, 225−230.
(59) Grabowska, E.; Reszczynska, J.; Zaleska, A. *Water Res.* **2012**, *46*, 5453−5471.
(60) Yu, J. G.; Yu, H. G.; Cheng, B.; Zhao, X. J.; Yu, J. C.; Ho, W. K. *J. Phys. Chem. B* **2003**, *107*, 13871−13879.
(61) Liu, G.; Niu, P.; Yin, L.; Cheng, H. M. *J. Am. Chem. Soc.* **2012**, *134*, 9070−9073.
(62) Liu, G.; Wang, L.; Sun, C.; Yan, X.; Wang, X.; Chen, Z.; Smith, S. C.; Cheng, H. M.; Lu, G. Q. *Chem. Mater.* **2009**, *21*, 1266−1274.
(63) Hirakawa, T.; Nosaka, Y. *Langmuir* **2002**, *18*, 3247−3254.